

Received 17 June 2025, accepted 8 July 2025, date of publication 14 July 2025, date of current version 22 July 2025.

Digital Object Identifier 10.1109/ACCESS.2025.3588817



Graph-Based Radiomics Feature Extraction From 2D Retina Images

OFÉLIO JORREIA[®]1, NUNO GONÇALVES^{®2,3}, (Member, IEEE), AND RUI CORTESÃO^{®2,3}, (Member, IEEE)

Department of Electrical and Computer Engineering, Institute of Systems and Robotics, University of Coimbra, 3030-290 Coimbra, Portugal

Corresponding author: Ofélio Jorreia (ofelio.jorreia@isr.uc.pt)

This work was supported by Fundação para a Ciência e a Tecnologia (FCT) under Grant PRT/BD/154310/2023 (DOI https://doi.org/10.54499/PRT/BD/154310/2023) and also by the FCT Project UID/00048, Institute of Systems and Robotics - Coimbra (ISR-UC).

ABSTRACT Medical image analysis offers valuable visual support for clinical decision-making, yet the incorporation of quantitative data is essential for deeper diagnostic insight. The radiomics approach addresses this need by combining quantitative image analysis with Machine Learning (ML) techniques, further enhancing Explainable Artificial Intelligence (XAI) for clinical applications. While working with two-dimensional (2D) images derived from volumetric data offers computational advantages, accurately estimating structural properties within these images remains challenging. Within the radiomics framework, this study introduces a methodology to distinguish bifurcations from other structural variations in 2D local fragments of retinal vasculature. Using a publicly available dataset of 29 retinal images, we extracted 1003 feature fragments for experiments. The regions of interest (ROIs) are identified using morphological image processing techniques. Specifically, candidate points are detected by applying structuring elements (SEs) to the skeletonized and binarized vasculature. From each candidate point, a local fragment of 35×35 pixels is extracted and used as input to the classification model. A Convolutional Neural Network (CNN) model, tailored for small image datasets and binary classification tasks is created. The trained model achieved an accuracy of 94.95% in correctly identifying bifurcation points. Based on predicted bifurcation points and blood vessel segments, we use the Graph-Based Radiomics Feature Extraction Algorithm (Graph-BRFExtract) to extract the adjacency matrix. This matrix serves as mathematical representation of the retinal vascular network, constituting a novel form of graph-based radiomic features.

INDEX TERMS Bifurcation, blood vasculature, explainable AI, graph-structured data, interpretability, radiomics, structuring element.

I. INTRODUCTION

The cardiovascular system addresses the heart, lungs, eyes, liver, brain and also the vascular network where blood flows. This network connects the above mentioned organs and provides oxygen and other nutrients to all tissues of the human body. Blood vasculature transport blood cells, nutrients, and oxygen to all tissues throughout the body. They also take waste and carbon dioxide away from tissues. This process is called blood flow. Blood vessels are essential for sustaining life, as all body tissues depend on

The associate editor coordinating the review of this manuscript and approving it for publication was Li Zhang .

their proper functioning [31]. Blood flow patterns of the cardiovascular system are important for accurate diagnosis of cardiovascular diseases [27], and can be inferred from blood vessel images [51]. In fact, cardiovascular diseases often have non-invasive diagnostic methods [46], [52], [53]. Some of these methods are based on medical imaging [8], [47], [82], [91]. Therefore, image-based accurate analysis is important, having drawn the attention of many researchers [26], [33], [69]. To apply network methods to blood vasculature, it is essential to extract nodes and edges. In this context, a network refers to the mathematical representation of a real-world complex system, defined by a collection of nodes (vertices) and their associated edges (links) [62]. Thus, we can consider

²Institute of Systems and Robotics, University of Coimbra, 3030-290 Coimbra, Portugal

³Department of Electrical and Computer Engineering, University of Coimbra, 3030-290 Coimbra, Portugal

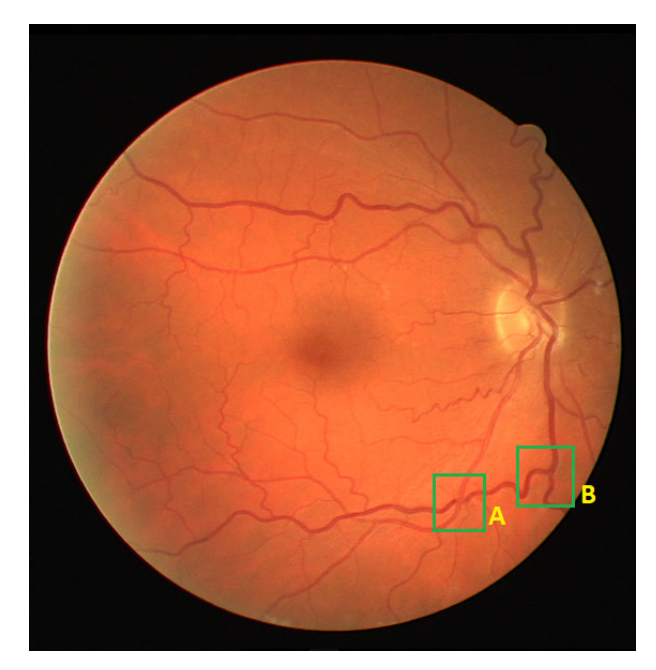


FIGURE 1. Retinal blood vessels. Region A shows an overlap of blood segments and region B shows a blood segment bifurcation [78].

bifurcation points of blood vessels as nodes and vessel segments as edges. In 2D blood vessel images, two possible scenarios can be observed at intersections:

- **Bifurcation** when the flow is divided into two or more segments in the case of arteries, or two or more segments come together in the case of veins.
- Overlapping when visually two or more vessel segments intersect. In certain observations, overlapping can be confused by bifurcation, resulting in false node or edge identification.

The in-depth analysis of medical images leads to radiomics methods, a quantitative approach to medical imaging that aims to detect image features through advanced and sometimes non-intuitive mathematical analysis [30], [42], [58]. There are several imaging modalities to visualize blood vessels, such as Computed Tomography (CT) [41], Magnetic Resonance Imaging (MRI) [36], Positron Emission Tomography (PET) [68], and Ultrasound [18], for instance. In these images, it is possible to detect similarities between blood vessels and a common network allowing to apply network approaches. As can be seen in Fig. 1, a random chosen image of the human retina shows a network of blood vessels exhibiting features that can be quantitatively analyzed. Bifurcations and overlaps can provide insights about blood related problems, although such characteristics are not always easy to identify. In 2D blood vessel imaging, overlapping of vessel segments may occur, resulting in incorrect detection of vessel bifurcation points, which is one of the key elements for mathematical network analysis. For instance, in the corresponding vasculature segmentation (see Fig. 2 obtained from Fig. 1), it is difficult or almost

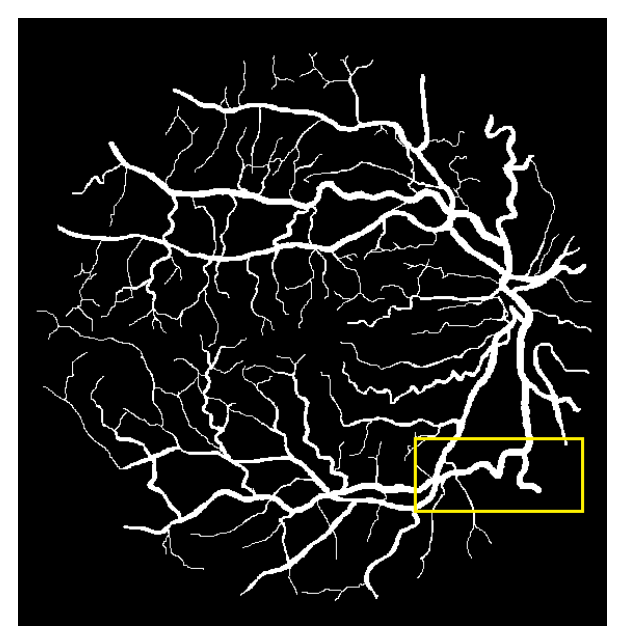


FIGURE 2. Binarized image of eye blood vessels. This is the vascular mask corresponding to Fig. 1 [78]. Both human vision and computer vision cannot distinguish whether some vessel intersections within the yellow rectangle belong or not to bifurcations.

impossible to identify whether points A and B are overlaps or bifurcations, respectively. It is also challenging to identify these points in regions with small vessels. Therefore, developing a Machine Learning (ML) classification model is needed for bifurcation identification. This work focuses on blood vasculature for radiomics feature extraction. The case study relies on 2D retina images. The background goal is to explore insights related to cardiovascular problems, by extracting network based features.

The paper is organized as follows: Section II describes available methods for radiomics, highlighting the new network radiomics feature. This section also includes a review of Explainable AI (XAI). Section III presents the proposed methodology, ranging from image preprocessing, fragment extraction in the Region of Interest (ROI) with target points (T-points), segmentation and conversion into classification data. In this section, we also present in detail the description of the classification model. Additionally, the method to extract the graph-based radiomics feature is discussed. Section IV shows the experimental results, highlighting the merits of the approach. Concluding remarks and contributions of this work are summarized in Section V, followed by future prospects and challenges.

The main contributions of this paper are as follows:

• We propose the Graph-Based Radiomics Feature Extraction Algorithm (Graph-BRFExtract Algorithm) to extract the (un)weighted adjacency matrix from retinal vasculature images and other medical images with vascular structures.



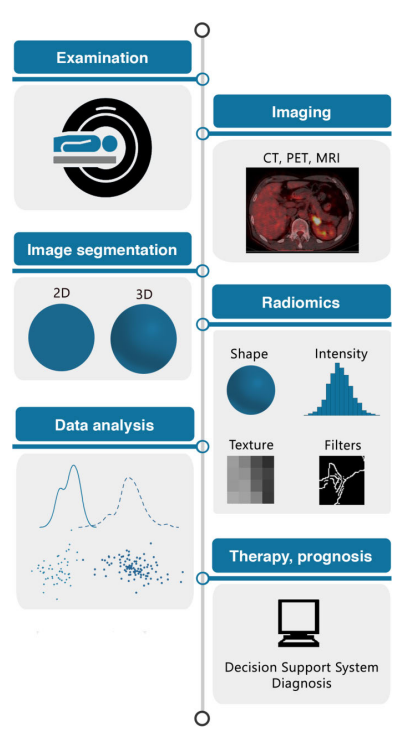


FIGURE 3. The radiomics workflow. Schematic illustration of the patient journey including image acquisition, analysis utilizing radiomics, and derived patient-specific therapy and/or prognosis [13], [30].

 Additionally, we introduce graph-based radiomics features from vasculature to enhance interpretable machine learning (IML) and explainable AI (XAI) frameworks.

II. RELATED WORK IN RADIOMICS

Radiomics analysis is the process of converting digital medical images into minable data. Data analysis through various statistical and mathematical processes allows quantification of various shape and textural characteristics referred to as radiomics features [13], [42], [57]. The concept of radiomics is based on the assumption that biomedical images contain information of disease-specific processes that is imperceptible to the naked eye and is not accessible through traditional visual inspection [3], [30]. Visual appreciable differences in image intensity, shape, or texture can be quantified by means of radiomics, thus overcoming the subjective nature of image interpretation, not implying diagnostic process automation [17]. It rather provides existing processes with additional data, as shown in Fig. 3, helping medical diagnosis. Among radiomics features described in [13], [42] and [46], the complex network approach we aim to focus on can be considered as a novelty radiomics feature. The new radiomics approach enables the extraction of points from medical images, allowing the analysis of their arrangement (constellation) and associated relationships. This method enables the exploration of patterns and insights related to cardiovascular problems.

A. INTERPRETABILITY AND GRAPH-STRUCTURED DATA

The graph theory, aligns well with complex network approach based on the modern theory of networks [28], [56], [87].

Graph-structured data are an integral part of many application domains, including chemoinformatics, computational biology, neuroimaging, and social network analysis [10], [23], [38], [48], [83]. Graphs allow modeling complex objects as a collection of entities (nodes) and of relationships between such entities (edges), each of which can be annotated by metadata such as categorical or vectorial node and edge features [44]. Graph data type representation is one of the most versatile data structures commonly employed in ML characterized to numerous applications benefit from the flexibility that it provide [11].

Understanding and interpreting the results of machine learning is of highest importance in the healthcare domain because the decision based on these predictions affect human lives. Therefore, algorithms or data should not bias the model when making decisions. XAI explains these results by highlighting critical features that domain experts can verify [4], [37], [63]. This ultimately helps to increase trust by providing transparency to these systems as they provide a human-understandable explanation of the results produced by the models. The drive for increased interpretability and explainability in ML models speak to the importance of transparency and trust in clinical settings [1], [63], [64], [81]. Making complex models that are more palatable to clinicians provides an opportunity for implementing machine learning insights properly and improve the process of decision-making with evidence-based and data-driven support [7], [16].

One of the ML steps is obviously the feature selection aiming to reduce irrelevant input data, increasing learning accuracy and improving comprehensibility. In recent years, data has become increasingly larger in both number of instances and number of features in many applications. This enormity may cause serious problems to many machine learning algorithms with respect to scalability and learning performance. Therefore, feature selection becomes very necessary for machine learning tasks when facing high dimensional data [50], [54], [86]. However, this trend of enormity on both size and dimensionality also poses severe challenges to feature selection algorithms. The graph can be used as derivative data type in radiomics for multimodal interpretation. Instead of using images as direct model inputs, features such as node-level attributes, edge weights, graph topological metrics (e.g., degree, centrality, and clustering coefficients), and subgraph patterns can provide valuable insights while reducing image feature dimensionality. The integration of this multimodal data sources with radiomic data processing enables a more comprehensive analysis of patient health, leading to a deeper understanding of disease mechanisms.

B. IMAGE PREPROCESSING FOR VASCULATURE EXTRACTION

In preprocessing stage, the delineation of the region/volume of interest (ROI/VOI) in two-dimensions (2D) or in three-dimensions (3D) is one crucial step of the pipeline [12],



[30]. ROIs/VOIs define regions in which radiomics features are calculated. Image segmentation might be manual, semiautomatic (using standard image segmentation algorithms such as region-growing or thresholding) [60], [85], or fully automated (nowadays, using deep learning algorithms) [21], [30]. However, the generalization of trained algorithms is currently a major limitation, since applying such algorithms on different datasets might entail very different results. Further research has to be devoted to develop robust and general algorithms for automated image segmentation. According to Van Timmeren et. al. [30] and Chaddad [13], image processing represents the attempt to homogenize images from which radiomics features are extracted, based on pixel spacing, gray-level intensities, bins of the graylevel histogram, and so forth. The robustness of these radiomics features largely depends on image processing settings [24], [76], such as device manufacturer [59], [70], intensity discretization [76], reproducibility [2], [13], number of iterations, post-filtering levels, input noise, reconstruction algorithms [6] and so forth. Therefore, each image processing step is important and must be adjusted to allow exposure of the vasculature depending on the image acquisition method (CT, MRI, PET).

In this study, we have used a retina image dataset. Eye images are extensively employed in medical research, with various techniques applied to clinical purposes [19], [51], [75], [89]. Many of these techniques align with imaging methods and use ML approaches. However, there is a notable lack of standardized frameworks [61], [76], [80], [90]. In this work, we emphasize the feature extraction for retinal image vascular quantification based on the radiomics approach.

III. METHODOLOGY

The journey of extracting the proposed network radiomics features involves identifying bifurcations in the retina vessel network through a ML classification model. Model development comprises three stages: 1) Acquisition and preprocessing of 2D retina images; 2) Feature extraction of T-points for classification; 3) Training, assessment and validation. The classification model is then used to identify bifurcations in retina images. Radiomics feature extraction involves representing bifurcations and adjacent blood vessels in the form of a graph adjacency matrix, enabling network-based analysis. Each stage is analyzed in the sequel.

A. STAGE 1: ACQUISITION AND PREPROCESSING

To perform this study, a set of 20 retina images from DRIVE¹ dataset with corresponding vasculature masks is analyzed. The dataset is provided for diagnosis, screening, treatment, and evaluation of various cardiovascular and ophthalmologic diseases such as diabetes, hypertension, arteriosclerosis and chorodial neovascularization. The images were acquired using a Canon CR5 non-mydriatic 3CCD camera with a

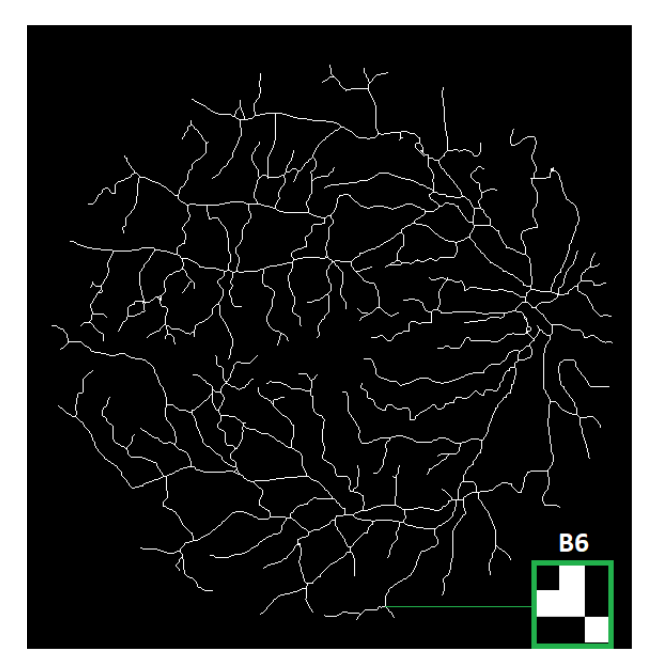


FIGURE 4. Binarized image skeleton of the retina vasculature. In this image the B6 structuring element fits on the T-point where the feature fragment (corresponding square fragment of 35×35 pixels on grayscale image) is going to be extracted.

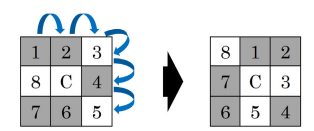


FIGURE 5. The SE is tilted clockwise by moving peripheral pixels to reproduce all possible shape forms.

45-degree field of view (FOV). Each image is captured at 768 × 584 pixels with 8 bits per color plane. The FOV of each image is circular, with a diameter of approximately 540 pixels. These images have been cropped around the FOV. Nine additional images, with a resolution of 2144×1424 pixels each, were added from Retinal Fundus Multi-disease Image Dataset (RFMiD),² bringing the total to 29 images. Before feature extraction analysis the images are converted to grayscale. Respective binary images representing retina vasculature masks do not explicitly distinguish between bifurcations and overlaps. By applying Zhang-Suen thinning algorithm [15] to skeletonize³ these masks, we reduce the vasculature thickness to a single pixel (Fig. 4). This allows the extraction of T-point coordinates using Structuring Elements (SEs) [55], [60]. The use of SEs helps to reduce noise and outliers in detecting potential T-points, overcoming known feature detection methods such as Harris corner detector [20], Min-Eigen corner detector and ORB (Oriented FAST Rotated BRIEF) corner detector [77], and facilitates accurate class assignment during feature fragment extraction by applying

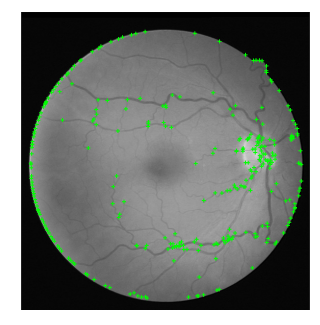
¹Provided by Kaggle: https://www.kaggle.com/datasets/andrewmvd/drive-digital-retinal-images-for-vessel-extraction

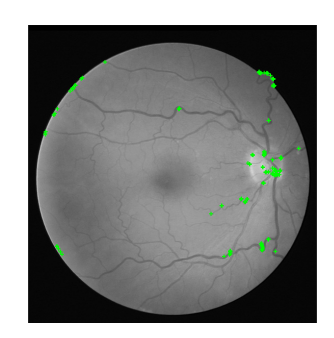
²Provided by Kaggle:https://www.kaggle.com/datasets/andrewmvd/retinal-disease-classification/data

³Morphological treatment of binary images that involves eroding objects reducing to a single pixel in thickness.

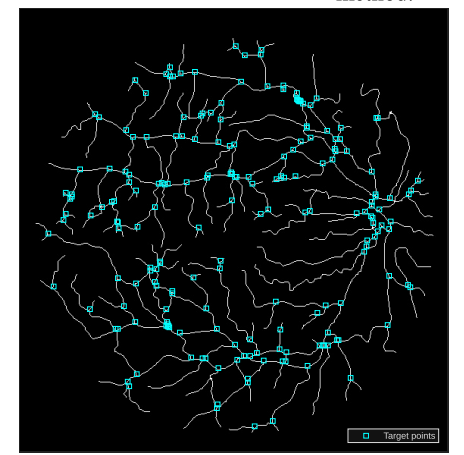


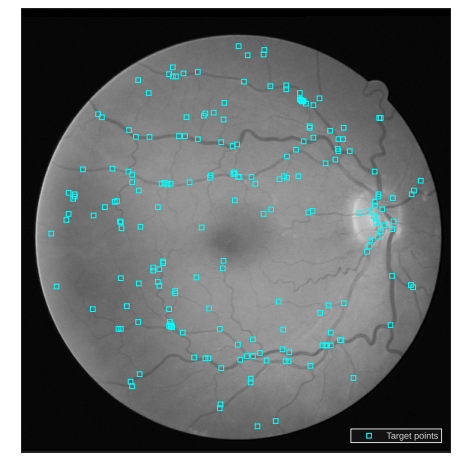






(a) Harris corner detector method. (b) Min-Eigen corner detector (c) ORB corner detector method. method.





(d) Skeletonized vasculature for coordinates extraction - proposed method.

(e) Proposed method for T-point detection.

FIGURE 6. T-points detection methods. a) Harris. b) Min-Eigen. c) ORB. d) and e) Proposed method.

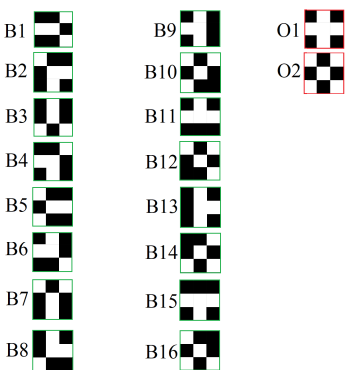




FIGURE 7. Set of 3×3 pixel structuring elements (SE) for T-point detection: bifurcation (left two columns) and overlap (third column).

them at intersections between vascular segments (Fig. 6). The coordinates are extracted by examining each pixel, row by row and column by column, over the skeletonized image. If a SE fits at a point along this path, the coordinates that match with the middle pixel of the SE are extracted. A set of 3×3 pixel SEs are defined to assign, as a first guess, the class each candidate point belongs to (1-for bifurcation in green and 0-for overlap in red), as can be seen in Fig. 7. In this task assignment, error may occur and therefore, visual

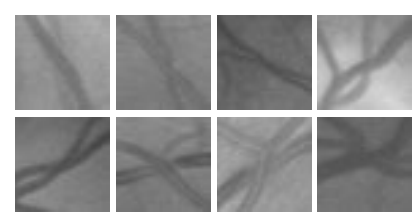


FIGURE 8. Fragments representing overlapping, noisy regions or other structural variations in the vasculature.

inspection is needed. It is important to note that the shapes of each column, starting from the second row (B2, B3,... and B10, B11,...), are the result of rotating previous shapes (Y-form B1 and T-form B9) clockwise by 45° and so forth. The SE is a binary square matrix with odd number of pixel per side, since the middle pixel (C in Fig. 5) of the square is used for coordinate extraction.

B. STAGE 2: FEATURE EXTRACTION FOR MODEL TRAINING

This stage involves extracting fragments from the retina image containing candidate points for bifurcation or not, through the coordinates defined in stage 1. The non-bifurcation clustering approach helps address situations like those illustrated in Fig. 8 (non-bifurcation points representing overlapping regions, noise or other structural variations in the vasculature), where T-points are unsuitable



for extracting fragments due to their geometry, making it difficult to determine whether they result from overlapping structures. This method can also be applied to thinner vessels. Recent studies by Mokan et al. [49], propose a segmentation method that differentiates veins from arteries and can be suitable in further works.

Using supervised ML approach, input data must be provided for model training [66]. Thus, through SEs and visual inspection, a set of 35×35 pixel feature fragments is extracted from grayscale images, segmented in gray-level thresholding and binarized to feed model predictors. For the binarization process, we applied local Otsu thresholding [72], meaning that Otsu's method was executed individually on each image fragment. This approach accounts for the spatial variability between fragments, such as differences in local intensity levels, even within the same retinal image. By employing a local thresholding strategy, we aim to minimize the extraction of noisy or inaccurate silhouettes, as demonstrated in Fig. 10.

The fragment size is chosen balancing region size and the proximity between T-points, aiming to collect as many features as possible. For training data, each feature fragment is then vectorized, resulting in a row input vector of 1225 (35 \times 35) elements (features). An additional element is appended to this vector, indicating the class it belongs to, based on the associated SE. This selection is done through visual inspection. Thus, each feature vector contains 1226 elements, and these vectors are grouped into a stack to form an input feature table for model training. In case of CNN the fragment is not vectorized and a class label vector is defined to represent the target categories for classification. CNNs include a layer called Flatten, which performs vectorization by converting multidimensional feature maps into a onedimensional vector. The table presents 1003 observations corresponding to feature fragments extracted from all retinal images, with 904 observations (90%) used for training and the remaining 10% set aside for model validation. The models are trained on incremental portions of the dataset - 25%, 50%, 75%, and 100% – to evaluate their performance based on the number of observations. It is important to note the features we refer to in this section are not the final radiomics features.

C. STAGE 3: MODEL TRAINING AND EVALUATION

To identify whether a T-point is a bifurcation or not, a classification model has to be created and trained to classify the corresponding fragments.

After identifying candidate points in all dataset images through the SEs, observations are grouped into two classes. Models are trained using 904 candidate points and associated pixel fragments, validated by visual inspection. In this work, the authors conduct visual inspections and manual annotations. Various ML algorithms suitable for classification tasks such as CNN, Decision Trees, K-Nearest Neighbour (KNN), Naive Bayes, Shallow Neural Networks and SVMs Classifiers, are trained and tested to create the classification model [66].

According to Martin-Isla [46], SVMs are frequently used in classification tasks related to image-based diagnosis. The SVM is a ML algorithm used for linear (standard SVM) or nonlinear classification, regression, and even outlier detection tasks [14], [74]. The main goal of the SVM algorithm is to compute the optimal hyperplane in an *n*-dimensional space that can separate data points in different classes in the feature space. The hyperplane is set so that the margin between the closest points of different classes should be as maximum as possible.

The SVM is extended to the nonlinear field by introducing a kernel function, becoming an effective method of nonlinear analysis [25]. In a SVM classifier, the kernel function is a crucial component, allowing the algorithm to handle nonlinear data relationships. It transforms input data into a higher-dimensional space where it becomes easier to separate classes using a hyperplane [29]. This transformation is known as "kernel trick" and it allows SVMs to create more complex decision boundaries without explicitly computing coordinates in high-dimensional spaces. Common kernel functions such as Gaussian Radial Basis Function (RBF) [67], polynomial and sigmoid have good performance in solving most of the problems due to good stability and wide adaptability.

Nonetheless, Convolutional Neural Networks (ConvNets or CNNs) have been proven very effective in areas such as image recognition and classification. Especially in the field of image classification, the CNN-based method has achieved excellent performance [35], [45]. As one of the most successful computer vision algorithms today, CNNs have been widely adopted as a core algorithm for image classification tasks [45]. In this work, we use a CNN architecture specifically designed for binary image classification. This network is particularly well-suited for small image datasets and straightforward classification tasks.

The best ML technique of this study is then used to estimate the class in which each point belongs to. The evaluation is performed using classification metrics that assess the overall performance [71]. These metrics are also used for model validation. The metrics are:

1) ACCURACY (Acc)

It measures the proportion of correct predictions made by the model out of all predictions. It is a fundamental evaluation metric, corresponding to the ratio of correctly predicted points to the total points in the dataset. The formula is:

$$Acc = \frac{TP + TN}{TP + FP + TN + FN} \tag{1}$$

where:

TP is the number of True Positive points; TN is the number of True Negative points; FP is the number of False Positive points; FN is the number of False Negative points.



2) PRECISION (Pr)

It is the proportion of true positive predictions among all positive predictions. It is a measure of how accurate positive predictions are. A high precision means the model has fewer false positives and the respective formula is:

$$Pr = \frac{TP}{TP + FP} \tag{2}$$

3) RECALL (Re)

It is also known as sensitivity or true positive rate (TPR), relating true positive predictions among all actual positive ones. It measures the classifier ability to identify points correctly. A high recall means few false negatives and is given by:

$$Re = \frac{TP}{TP + FN} \tag{3}$$

4) F₁SCORE

It is the harmonic mean of precision and recall, providing a metric that balances both measures. It is beneficial when dealing with imbalanced datasets, where one class is significantly more frequent than the other. The formula for the F_1S core is:

$$F_1Score = \frac{2}{\frac{1}{P_r} + \frac{1}{Re}} = 2 \times \frac{Pr \times Re}{Pr + Re}$$
 (4)

5) CONFUSION MATRIX

This matrix, also known as an error matrix, evaluates the performance of classification models in ML and statistics. It provides a summary of the predictions made by a classifier compared to the actual class labels, enabling a detailed analysis and comprehensive view of the classifier performance across different classes. It helps identify misclassification patterns.

D. GRAPH-STRUCTURED DATA EXTRACTION

Radiomics features are broadly categorized based on their characteristics and the aspects of the image they describe. Common categories include shape-based features [9], first-order statistical features (intensity-based features) [39], and texture-based features [65]. In this study, we employ a graph-based approach, using medical images that reveal blood vessels to extract the vascular network, introducing a new category within radiomics beyond the traditional ones mentioned.

Identifying bifurcations is a well-established task, with recent work by Long et al. [43], demonstrating increasing accuracy in this area. However, in this study, we go further by proposing the extraction and numerical representation of graph-based features. Similar network features are frequently used in neuroimaging for analyzing brain diseases such as Alzheimer's disease [34]. To the best of our knowledge, in the field of clinical imaging, the adjacency matrix is commonly employed for brain network analysis, representing connectivity between regions of interest (ROIs) [32], [40]. These

Algorithm 1: Graph-BRFExtract Algorithm

```
1 begin;
2 load images;
  /\star loading image for coordinates extraction,
     SEs and target image in gray scale
3 detect and save T-points in a vector n;
4 define adjacency matrix W as square
   matrix with size n and zero elements;
    // n is the number of T-points
5 for T-point i = 1 : n do
      extract and classify fragment in
       T-point i;
7
      if T-point i is a bifurcation then
8
         for T-point j = 1 : n do
             extract and classify fragment
              in T-point j;
             if T-point j is a bifurcation then
10
                for segment k = 1 : v do
                    /* v is the number of vessel
                       segments
                    if T-point i, T-point j and segment k
12
                     are connected then
                       \mathbf{W}_{ij} = 1
                        /* in weighted adjacency
                           matrix \mathbf{W}_{ij} = w_{ij} where
                           w_{ii} is corresponding to
                           v_k vessel thickness
14 save matrix W;
15 end.
```

connections are derived from Pearson correlation coefficients when brain voxels (ROIs) defined by an anatomical brain map are activated. This activation occurs through a process known as BOLD (Blood Oxygen Level Dependent) imaging [34], [79], [92].

In radiomics, feature extraction refers to calculations, where feature descriptors are used to quantify characteristics of pixel spacing, gray-level intensities, bins of the gray-level histogram, and so forth, within the ROI. Since many different ways and formulas exist [22], [42], [84], the Graph-BRFExtract Algorithm (Alg. 1) is based on the following graph representation:

$$G = (V, E), \tag{5}$$

where V is a set of nodes, and E is a set of edges between nodes, i.e.,

$$E \subseteq \{(u, v)|u, v \in V\}. \tag{6}$$

In this context, we are dealing with a binary graph, meaning there is no weight information associated with the edges of the graph [34]. $\mathbf{W} \subseteq R^{N \times N}$ is the adjacency (or weight) matrix for a graph G, where $\mathbf{W}_{ij} = 1$ if there is an edge between nodes i and j; otherwise, $\mathbf{W}_{ij} = 0$. N is the number of nodes in G.

The assigned SEs of class 1 for bifurcation and 0 for not bifurcation are compared with T-points for evaluation. If the



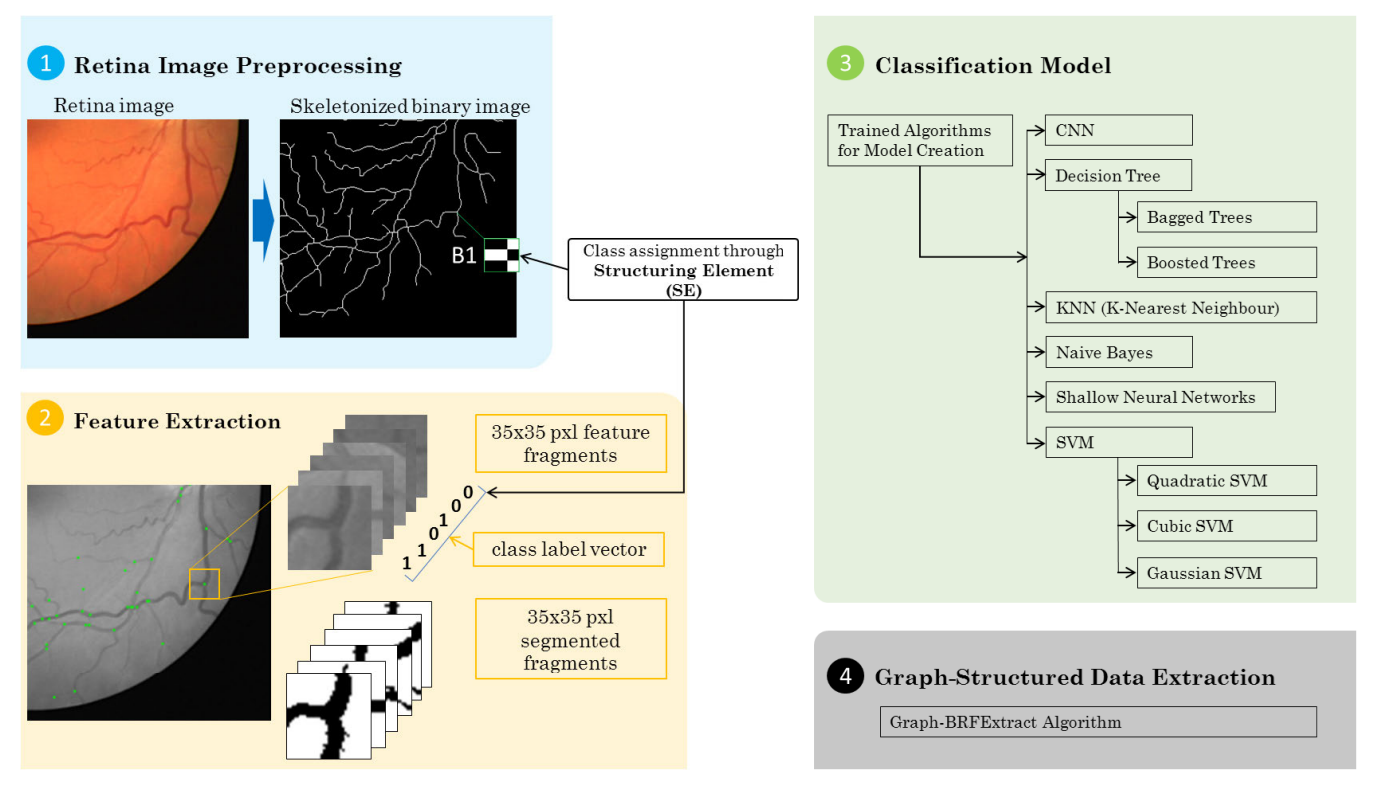


FIGURE 9. Representation of the three-stage classification process before graph-structured data extraction: In the first stage, the images are homogenized, and the vasculature is converted into a binary representation. The second stage focuses on extracting feature fragments from detected T-points, with each fragment sized at $n = 35 \times 35$ pixels. These fragments are then segmented for further analysis. The final stage involves developing and training ML models using appropriate algorithms for classification. Image preprocessing and feature extraction are carried out in MATLAB R2023b, while the classification stage is implemented using both MATLAB R2023b Classification Learner and Python 3.11.7.

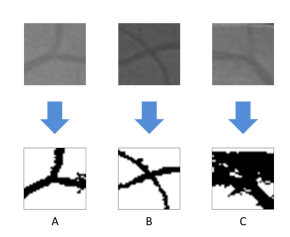


FIGURE 10. Frame segmentation. From left to right: A - segmented bifurcation; B - segmented overlap; and; C - noisy segmented bifurcation.

SE fits, i.e., if each of the pixels in the SE is associated with the corresponding pixel of the neighborhood under the SE at any point in the skeletonized image, the coordinates of the middle pixel of the SE at that point, are extracted. These coordinates are then used as the middle point of the feature fragment to be extracted in the gray scale image. Then, the feature fragment is segmented and binarized as described in Sect. III-B. In this work, we use a two-class classification approach: one class groups bifurcations, and the other one includes non-bifurcations, overlaps, and noisy fragments. Therefore, as can be seen in Fig. 10, extracting fragments can result in some noisy features. Finally, the resulting feature fragment is classified. If the target classification output is 1, then it belongs to a bifurcation and is considered a graph node.

Fig. 9 depicts the classification process to identify bifurcation points in retina images. The identified points, along

with their respective adjacent blood vessels, are represented as an adjacency matrix - a mathematical representation of a graph or network. This constitutes the new network radiomics feature.

IV. EXPERIMENTS

The experiments are conducted to validate the proposed methodology and identify the most suitable algorithms for developing the classification model. The tests followed the three stages outlined in section III and were conducted across multiple computers running MATLAB R2023b and Python 3.11.7, with parameters optimized to best fit each algorithm. The training data is algorithm-independent, ensuring that the same dataset is utilized for training Decision Tree, KNN, Naive Bayes, Shallow Neural Networks, and SVM models, with the exception of CNN, which requires a different input structure. Given its focus on computer vision, the training data for the CNN algorithm is prepared as binarized fragments of 35×35 pixels.

A. SELECTED MODEL

All experiments in this study are carried out using image processing and ML classification toolboxes in both MATLAB R2023b and Python 3.11.7. Metrics are calculated from confusion matrices, based on output data after training, by applying 5-fold cross-validation on randomly separated data, with 10% set aside for model testing.



TABLE 1. Values used for the grid search to determine the optimal parameters for the CNN classification model, including activation functions: parametric ReLU (PReLU) and leaky ReLU (LeakyReLU).

CNN Layer	Parameter list
Conv2D1	[sigmoid, relu, softmax, leaky-relu, parametric relu]
Conv2D2	[sigmoid, relu, softmax, leaky-relu, parametric relu]
Dense1	[sigmoid, relu, softmax, leaky-relu, parametric relu]
Dense2	[sigmoid, relu, softmax]
Dropout1	[0.2, 0.3, 0.4, 0.5]
Dropout2	[0.2, 0.3, 0.4, 0.5]
Dropout3	[0.2, 0.3, 0.4, 0.5]
Learning parameters	Parameter list
Learnig rate	$[1 \times 10^{-2}, 1 \times 10^{-3}, 1 \times 10^{-4}]$
Convolution kernel Size	[(3,3),(7,7),(9,9),(11,11),(15,15),(17,17),(19,19)]

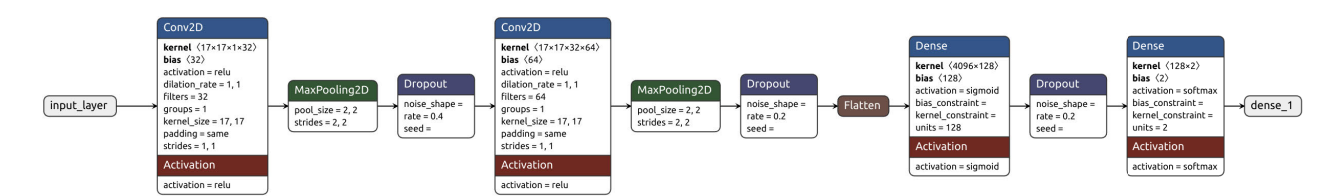


FIGURE 11. This diagram illustrates the architecture of the trained CNN classification model used for bifurcation detection. The first layer, with $n = 35 \times 35 = 1225$, represents the number of input features, corresponding to the total pixels per fragment. The network is implemented in Python, and the diagram is generated using Netron 8.2.1.

TABLE 2. Validation confusion matrices of best performing models.

		CNN			Cubic SVM Predictions		
		0	1			0	1
Actual	0	50	4	mal	0	49	2
Act	1	3	42	Act	1	1	47
Quadratic SVM Predictions				Gaussian SVM Predictions			
		0	1			0	1
ual	0	50	1	ual	0	48	3
 Actual	1	2	46	Actua	1	2	46

Table 4 presents results for the best performing classifier models. Among the trained ML algorithms, SVMs and CNN demonstrated better accuracy. The CNN approach produces the best results, overall. The graph in Fig. 12 illustrates its training progression, showing validation accuracy values stabilizing above 90%. An analysis of the graphs in Figs. 13 and 14 clearly indicates that the accuracy of the CNN model increases with the number of training observations. In contrast, the SVM models do not exhibit significant performance gains with increased training data but demonstrate stable accuracy even with a relatively smaller number of observations.

For the present experiment a 12-layer CNN, including input and output layers, was constructed (Fig. 11). Table 1 outlines the set of parameters employed in the grid search process for training the classification network. The objective is to fine-tune the model to identify the optimal parameter configuration. The CNN architecture

TABLE 3. The total number of trainable parameters in the CNN classification model is summarized below.

		Number of
CNN Layer (type)	Output Shape	Parameters
conv2d (Conv2D)	(None, 35, 35, 32)	9,280
max_pooling2d		
(MaxPooling2D)	(None, 17, 17, 32)	0
dropout (Dropout)	(None, 17, 17, 32)	0
conv2d_1 (Conv2D)	(None, 17, 17, 64)	591,936
max_pooling2d_1		
(MaxPooling2D)	(None, 8, 8, 64)	0
dropout_1 (Dropout)	(None, 8, 8, 64)	0
flatten (Flatten)	(None, 4096)	0
dense (Dense)	(None, 128)	524,416
dropout_2 (Dropout)	(None, 128)	0
dense_1 (Dense)	(None, 2)	258

comprises convolutional, dropout, flatten, and dense layers, each characterized as follows:

– The first convolutional layer (Conv2D1) extracts low-level features from input fragments, followed by a max pooling layer (MaxPooling2D) that reduces the spatial dimensions. This pooling operation is repeated after the second convolutional layer (Conv2D2) to further downsample the feature maps. To prevent overfitting, dropout layers (Dropout1, Dropout2, and Dropout3) are incorporated, randomly deactivating a subset of neurons during training. After the convolutional process, the flatten layer transforms the 2D feature maps into a one-dimensional vector. Subsequently, a fully connected layer with 128 neurons (Dense1) captures high-level abstractions, while the final fully connected layer (Dense2) outputs class probabilities for classification.

To ensure optimal model tuning, training was conducted using the parameters summarized in Table 3:



TABLE 4. Results of the best performing classifier models. In this table 100% of dataset is corresponding to 1003 observations and 25%, 50% and 75%
are respectively 251, 501 and 752 observations.

Trained models	Observations (%)	Accuracy (%)	Precision (%)	Recall (%)	F ₁ Score (%)
	25	72.00	72.00	72.00	72.00
CNN	50	83.67	83.67	83.67	83.67
	75	85.71	85.71	85.71	85.71
	100	94.95	94.95	94.95	94.95
	25	78.76	75.23	79.61	77.73
Cubic SVM	50	84.26	82.13	83.33	82.36
	75	85.97	84.19	85.02	84.60
	100	85.60	83.33	85.37	84.34
	25	78.32	73.68	81.55	77.42
Quadratic SVM	50	84.48	81.31	85.29	83.25
	75	84.19	81.65	84.04	82.83
	100	85.60	83.18	85.61	84.38
	25	76.55	74.04	74.76	74.40
Gaussian SVM	50	86.47	83.89	86.76	85.30
	75	87.30	85.30	86.97	86.13
	100	87.38	86.10	86.10	86.10

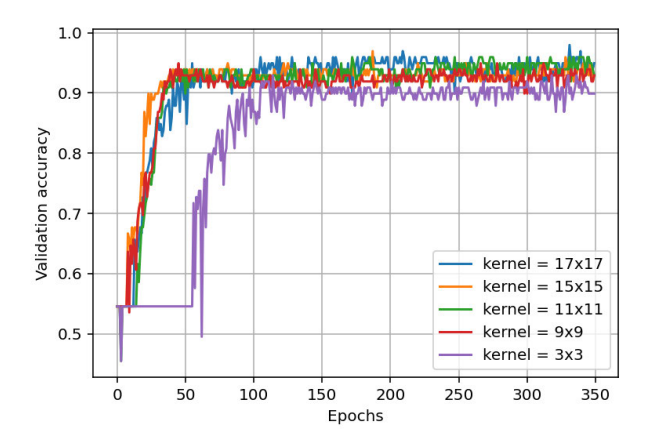


FIGURE 12. CNN model performance when trained on the full dataset using all available observations. The figure highlights the influence of convolutional kernel size, with the 17 \times 17 kernel yielding the best classification performance.

- Conv2D1 activation function: relu;
- Conv2D2 activation function: relu;
- dense layer Dense1 activation function: sigmoid;
- dense layer Dense2 activation function: softmax;
- dropout layer Dropout1 parameter: 0.2;
- dropout layer Dropout2 parameter: 0.2;
- dropout layer Dropout3 parameter: 0.4;
- Learning rate: 1×10^{-3} ;
- Convolutional kernel size: 17 × 17.

B. GROUND TRUTH AND DISCUSSION

Fig. 15 graphically highlights the performance of our method. It can be inferred that retina images typically have more bifurcations than overlapping vessel segments. In certain cases, these segment crossings are mistakenly seen as bifurcations in regions where vessels are thin. Additionally, T-points that are very close to each other can result in the extraction of similar, overlaid, or identical feature fragments. These issues affect model performance. For instance, consider the sample image shown in Fig. 15a. Using the proposed SEs, 68 out

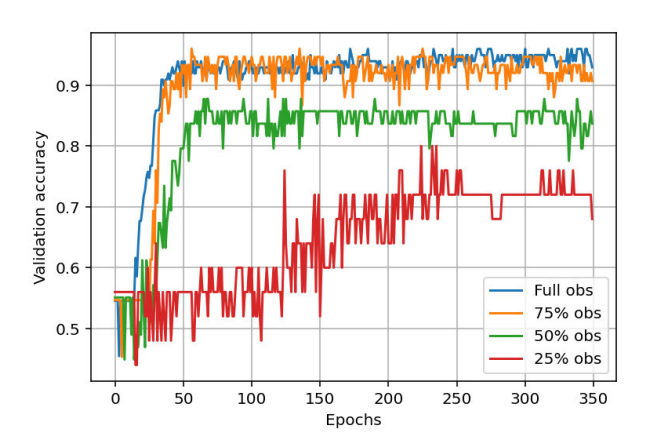


FIGURE 13. The CNN model shows a consistent improvement in accuracy as the number of observations in the dataset increases.

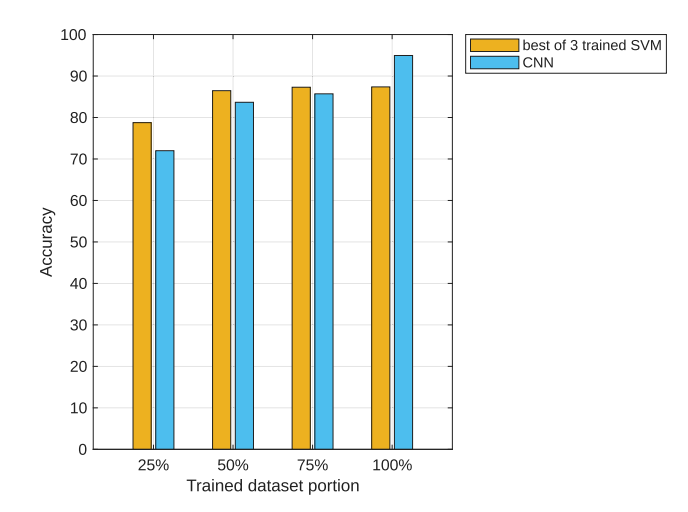


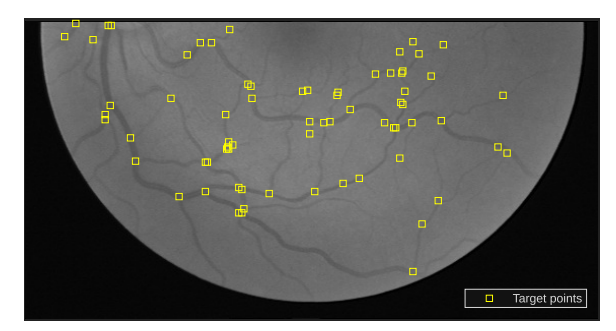
FIGURE 14. The CNN model shows a notable improvement as the dataset grows, highlighting its capacity to leverage larger amounts of data. In contrast, the SVM model achieves stable accuracy with a relatively smaller number of observations.

of 69 T-points are identified (Fig. 15b). The coordinates of these points are represented in the grayscale image (see Fig. 15c), where feature fragments are extracted to classify

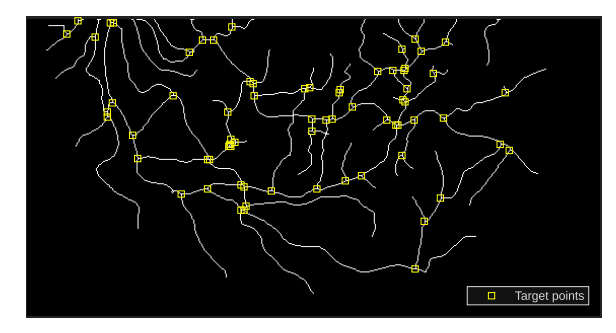




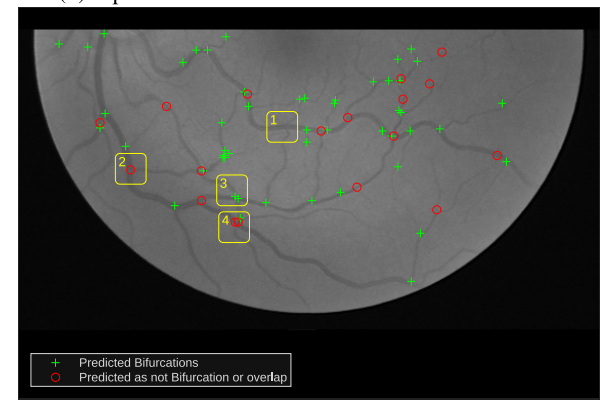
(a) Sample RGB image of retinal blood vessel.



(c) T-points overlayed on the grayscale image.



(b) T-points on the vessel skeleton defined with SEs.



(d) Prediction outcome. The yellow squares were manually annotated through visual inspection, highlighting regions where misclassification occurred or where the classifier exhibited performance issues.

FIGURE 15. T-points predictions. a) Unprocessed retina image. b) Vasculature mask of the sample image after skeletonization and T-points detection using SE's. c) Coordinates on the graycale image where feature fragments are extracted. d) Green points are identified as bifurcations and red circles as not bifurcations by the classification model.

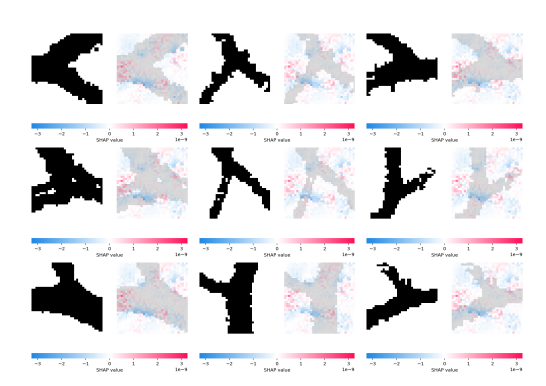


FIGURE 16. Explaining CNN model utilizing SHAP: evaluating nine fragment samples. The regions in red represent positive impact pixels for model accuracy; as same as blue regions shows negative impact regions. Thus, the peripheral regions of the fragment play a key role in the model's accuracy.

each point as a bifurcation or not. As a demonstrative example, the Fig. 15d illustrates the best-performing SVM model classifying 50 points as bifurcations and the remaining 18 as non-bifurcations. In this image, some misclassification errors can be observed through visual inspection, which may be related to the proximity between T-points, model accuracy and issues with vessel thicknesses.

TABLE 5. Confusion matrix associated to Fig. 15.

	Sample image	Predicted	
	prediction outcome	0	1
nal	0	12	7
Actı	1	6	43

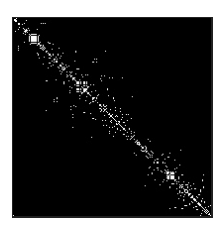
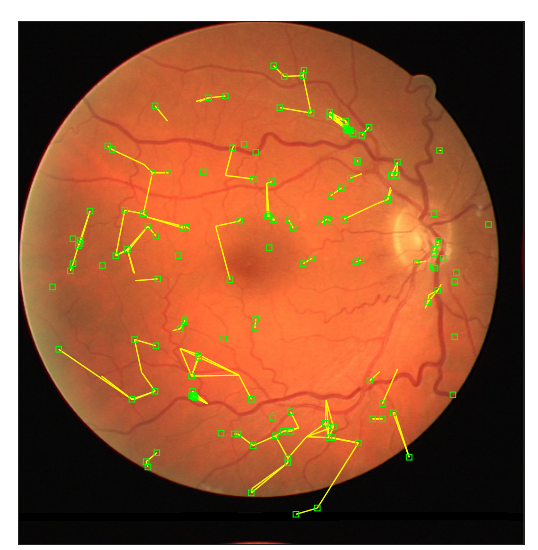
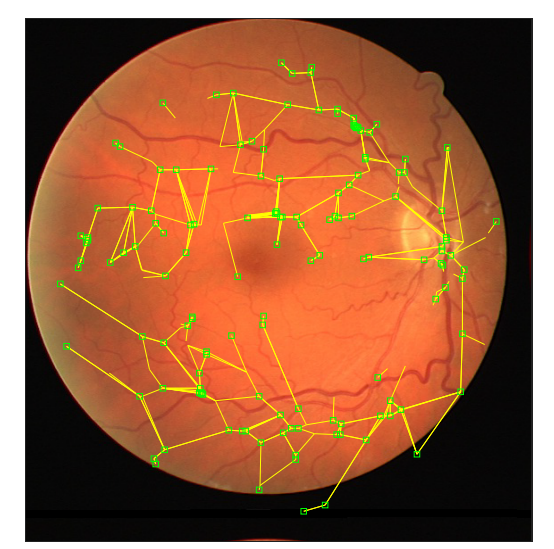


FIGURE 17. Unweighted adjacency matrix W between 201 nodes from predicted bifurcation points, corresponding to Fig. 1, represented as a binary image. Each white dot represents adjacency = 1 between each pair of nodes.

The four regions within the yellow squares in Fig. 15d are manually defined to highlight specific issues to be addressed by the classifier. All T-points are detected using SEs except the one in region 1, resulting in a 98.55% detection rate of the method we propose. Region 2 illustrates a misclassification error: visual observation indicates that



(a) The graph overlay on the corresponding eye retina image highlights the vascular structure. Gaps in segment reconstruction are primarily caused by vessel overlap at crossing points and model misclassification of bifurcations.



(b) Graph representation using the best-performing model.

FIGURE 18. Graph overlay on corresponding eye retina image. The green points represent predicted bifurcations and the yellow lines represent the adjacency resulting in an unweighted graph – the network radiomics feature – This is performed in MATLAB R2023b.

this point is a bifurcation, but the classifier identified it as not a bifurcation. Region 3 shows the identification of two bifurcation points resulting from two T-points being identified after wide vessel skeletonization (see Fig. 15b), leading to the extraction of two partially overlapping feature fragments and subsequent misclassification. Finally, region 4 demonstrates correct classifier identification of both bifurcation and non-bifurcation in a region where T-points are close together.

In summary, Table 5 presents the classification confusion matrix associated to Fig. 15. The following performance metrics are obtained: Acc = 80.88%, Pr = 86%, Re = 87.76%, and F₁Score = 86.87%.

Aiming to understand the CNN classifier behavior on fragment pixels through explainable AI, SHapley Additive exPlanations (SHAP) method [5], [73] is applied to a set of 9 sampled fragments from test data. This is a Post Hoc explanation method that provides a means to interpret and understand model behavior and which pixels are relevant for the classifier [63], [88]. These values can indicate both positive impacts (in red) and negative impacts (in blue), on the output in peripheral pixel clusters of the fragments in Fig. 16.

C. VESSEL NETWORK ADJACENCY MATRIX EXTRACTION

After identifying bifurcation points, the adjacency matrix W is calculated. In this matrix, each element a_{ij} denotes the connection between the i^{th} row and the j^{th} column. Fig. 17 visually represents the adjacency matrix corresponding to the 201 nodes identified in the retina image, illustrating as white dots the presence of edges between estimated nodes. This results in a symmetric square matrix extracted

by Algorithm 1. Additionally, each T-point is connected to itself when classified as a bifurcation. These identified bifurcations are then treated as nodes for constructing a graph that represents the retinal vascular network. Fig. 18 illustrates the generated graph derived from the adjacency matrix, where edges represent individual blood vessel segments.

V. CONCLUSION

This work addresses radiomics for retina images. It focuses on identifying bifurcations using a ML classifier. To distinguish bifurcations from non-bifurcations, 18 SEs are defined and 1003 local observations of 35 × 35 pixel fragments are extracted at each T-point for classifier input. Various ML classification algorithms have been trained, with CNN demonstrating the best accuracy (94.95%). Widely used in computer vision, the CNN model demonstrates improved accuracy with larger datasets and, in this work, is particularly notable for its suitability in classifying small image fragments. The Graph-BRFExtract Algorithm is employed to quantify identified bifurcations by representing them as an adjacency matrix, extending beyond traditional radiomics features [13]. This matrix captures the topology and patterns of the vascular network, offering valuable insights that can support cardiovascular clinical decision-making. This approach enables to overcome the closed box nature of ML models, providing deeper insights into algorithms through data-driven Explainable AI (XAI) and further research may involve exploring properties of the retina vascular representation to discern characteristics of cardiovascular abnormalities within the domain of topological network analysis. In this context, the weights of connectivity between bifurcation



points, equivalent to vessel thicknesses, may be considered. In this study, we observed that the inherent heterogeneity of the image acquisition process may present significant challenges to the generalizability and reproducibility of the proposed methodology. Additionally, gray-scale intensity and texture characteristics can be investigated to separate arterial from venous vessels, enabling the distinction between these two networks through segmentation techniques.

REFERENCES

- J. Abrantes and P. Rouzrokh, "Explaining explainability: The role of XAI in medical imaging," Eur. J. Radiol., vol. 173, Apr. 2024, Art. no. 111389.
 [Online]. Available: https://www.sciencedirect.com/science/article/pii/S0720048X24001050
- [2] B. A. Altazi, G. G. Zhang, D. C. Fernandez, M. E. Montejo, D. Hunt, J. Werner, M. C. Biagioli, and E. G. Moros, "Reproducibility of F18-FDG PET radiomic features for different cervical tumor segmentation methods, gray-level discretization, and reconstruction algorithms," *J. Appl. Clin. Med. Phys.*, vol. 18, no. 6, pp. 32–48, Nov. 2017, doi: 10.1002/acm2.12170. [Online]. Available: https://aapm.onlinelibrary.wiley.com/doi/abs/10.1002/acm2.12170
- [3] M. Amini, I. Shiri, and H. Zaidi, "PET and CT information fusion and quality assessment toward optimized radiomic features extraction," in Proc. IEEE Nucl. Sci. Symp. Med. Imag. Conf. (NSS/MIC), Nov. 2022, pp. 1–3.
- [4] A. Avinash, A. Harikumar, A. Nair, S. K. Pai, S. Surendran, and L. George, "A comparison of explainable AI models on numeric and graph-structured data," *Proc. Comput. Sci.*, vol. 235, pp. 926–936, Jan. 2024. [Online]. Available: https://www.sciencedirect.com/science/article/pii/S1877050924007646
- [5] N. Baig, S. I. Abba, J. Usman, I. Muhammad, I. Abdulazeez, A. G. Usman, and I. H. Aljundi, "Bio-inspired MXene membranes for enhanced separation and anti-fouling in oil-in-water emulsions: SHAP explainability ML," *Cleaner Water*, vol. 2, Dec. 2024, Art. no. 100041. [Online]. Available: https://www.sciencedirect.com/science/article/pii/S2950263224000395
- [6] C. Bailly, C. Bodet-Milin, S. Couespel, H. Necib, F. Kraeber-Bodéré, C. Ansquer, and T. Carlier, "Revisiting the robustness of PET-based textural features in the context of multi-centric trials," *PLoS ONE*, vol. 11, no. 7, Jul. 2016, Art. no. e0159984, doi: 10.1371/journal.pone.0159984.
- [7] M. Balamurugan, M. S. Muthuraman, V. Porkodi, M. Sivaram, M. Sridharan, and E. Gangadevi, "Combining graph theory and machine learning for network-based medical image analysis," in *Proc. Int. Conf. Trends Quantum Comput. Emerg. Bus. Technol.*, Mar. 2024, pp. 1–5.
- [8] Y. Benxian, Z. Yufeng, H. Bingbing, and Y. Ruihan, "Doppler ultrasound blood flow velocimetry based on the optimization of effective EEMD components," in *Proc. IEEE 6th Int. Conf. Comput. Commun. (ICCC)*, Dec. 2020, pp. 1181–1185.
- [9] N. A. Bhalchandra, R. Prashanth, S. D. Roy, and S. Noronha, "Early detection of Parkinson's disease through shape based features from 123Iioflupane SPECT imaging," in *Proc. IEEE 12th Int. Symp. Biomed. Imag.* (ISBI), Apr. 2015, pp. 963–966.
- [10] D. B. Blumenthal, N. Boria, S. Bougleux, L. Brun, J. Gamper, and B. Gaüzère, "Scalable generalized median graph estimation and its manifold use in bioinformatics, clustering, classification, and indexing," *Inf. Syst.*, vol. 100, Sep. 2021, Art. no. 101766. [Online]. Available: https://www.sciencedirect.com/science/article/pii/S0306437921000284
- [11] K. Borgwardt, E. Ghisu, F. Llinares-Lopez, L. O'Bray, and B. Rieck, Graph Kernels: State-of-the-Art and Future Challenges, 2020.
- [12] A. Chaddad, "Stability in radiomics analysis: Advancements and challenges," in *Proc. IEEE Int. Conf. E-Health Netw., Appl. Services* (Healthcom), Dec. 2023, pp. 1–5.
- [13] A. Chaddad and X. Liang, "Stability of radiomic models and strategies to enhance reproducibility," *IEEE Trans. Radiat. Plasma Med. Sci.*, vol. 8, no. 5, pp. 540–555, May 2024.
- [14] F. F. Chamasemani and Y. P. Singh, "Multi-class support vector machine (SVM) classifiers—An application in hypothyroid detection and classification," in *Proc. 6th Int. Conf. Bio-Inspired Computing: Theories Appl.*, Sep. 2011, pp. 351–356.

- [15] W. Chen, L. Sui, Z. Xu, and Y. Lang, "Improved Zhang-Suen thinning algorithm in binary line drawing applications," in *Proc. Int. Conf. Syst. Informat. (ICSAI)*, May 2012, pp. 1947–1950.
- [16] M. Dou, H. Liu, Z. Tang, L. Quan, M. Xu, F. Wang, Z. Du, Z. Geng, Q. Li, and D. Zhang, "Non-invasive classification of non-neoplastic and neoplastic gallbladder polyps based on clinical imaging and ultrasound radiomics features: An interpretable machine learning model," Eur. J. Surgical Oncol., vol. 51, no. 6, Jun. 2025, Art. no. 109709. [Online]. Available: https://www.sciencedirect.com/science/article/pii/S0748798325001374
- [17] V. Eleftheriadis, J. R. H. Camacho, V. Paneta, B. Paun, C. Aparicio, V. Venegas, M. Marotta, M. Masa, G. Loudos, and P. Papadimitroulas, "Radiomics and machine learning for skeletal muscle injury recovery prediction," *IEEE Trans. Radiat. Plasma Med. Sci.*, vol. 7, no. 8, pp. 830–838, Jul. 2023.
- [18] B. S. Generowicz, L. Verhoef, F. Mastik, S. Dijkhuizen, N. v. Dorp, J. Voorneveld, J. G. Bosch, K. Kumar, G. Leus, C. I. D. Zeeuw, S. K. E. Koekkoek, and P. Kruizinga, "Vector Doppler imaging of small vessels using directionally filtered power Doppler images," in *Proc. IEEE Int. Ultrason. Symp. (IUS)*, Sep. 2020, pp. 1–4.
- [19] C. Gong, N. B. Erichson, J. P. Kelly, L. Trutoiu, B. T. Schowengerdt, S. L. Brunton, and E. J. Seibel, "RetinaMatch: Efficient template matching of retina images for teleophthalmology," *IEEE Trans. Med. Imag.*, vol. 38, no. 8, pp. 1993–2004, Aug. 2019.
- [20] S. Guiming and S. Jidong, "Multi-scale Harris corner detection algorithm based on Canny edge-detection," in *Proc. IEEE Int. Conf. Comput. Commun. Eng. Technol. (CCET)*, Aug. 2018, pp. 305–309.
- [21] C. Guo, M. Szemenyei, Y. Yi, W. Wang, B. Chen, and C. Fan, "SA-UNet: Spatial attention U-net for retinal vessel segmentation," 2020, arXiv:2004.03696.
- [22] C. Haarburger, J. Schock, D. Truhn, P. Weitz, G. Mueller-Franzes, L. Weninger, and D. Merhof, "Radiomic feature stability analysis based on probabilistic segmentations," in *Proc. IEEE 17th Int. Symp. Biomed. Imag. (ISBI)*, Oct. 2020, pp. 1188–1192.
- [23] Y. Hao, X. Wang, L. Li, M. Zhang, and L. Chang, "A dynamic social network graph anonymity scheme with community structure protection," *Comput., Mater. Continua*, vol. 82, no. 2, pp. 3131–3159, 2025. [Online]. Available: https://www.sciencedirect.com/ science/article/pii/S1546221825000980
- [24] X. He, Z. Chen, Y. Gao, W. Wang, and M. You, "Reproducibility and location-stability of radiomic features derived from cone-beam computed tomography: A phantom study," *Dentomaxillofacial Radiol.*, vol. 52, no. 8, Nov. 2023
- [25] S. Huishu, Z. Yi, and S. Ye, "Multi-scale Cauchy kernel function and its application in multi-class SVM," in *Proc. 5th Int. Conf. Instrum. Meas.*, *Comput., Commun. Control (IMCCC)*, Sep. 2015, pp. 1156–1160.
- [26] N. U. Häner, C. Dysli, and M. R. Munk, "Imaging in retinal vascular disease: A review," *Clin. Experim. Ophthalmology*, vol. 51, no. 3, pp. 217–228, Apr. 2023, doi: 10.1111/ceo.14203. [Online]. Available: https://onlinelibrary.wiley.com/doi/abs/10.1111/ceo.14203
- [27] IPSOS. (Sep. 30, 2023). Actual and Public Estimates of Causes of Death Worldwide As of 2019. [Online]. Available: https://www.statista.com/statistics/1108748/cause-of-death-estimate-and-actual-worldwide/
- [28] L. E. Ismail and W. Karwowski, "A graph theory-based modeling of functional brain connectivity based on EEG: A systematic review in the context of neuroergonomics," *IEEE Access*, vol. 8, pp. 155103–155135, 2020.
- [29] U. Jain, K. Nathani, N. Ruban, A. N. Joseph Raj, Z. Zhuang, and V. G. V. Mahesh, "Cubic SVM classifier based feature extraction and emotion detection from speech signals," in *Proc. Int. Conf. Sensor Netw. Signal Process. (SNSP)*, Oct. 2018, pp. 386–391.
- [30] J. E. van Timmeren, D. Cester, S. Tanadini-Lang, H. Alkadhi, and B. Baessler, "Radiomics in medical imaging—'How-to' guide and critical reflection," *Insights Imag.*, vol. 11, no. 1, Dec. 2020, doi: 10.1186/s13244-020-00887-2.
- [31] G. Jayalalitha, V. Shanthoshini Deviha, and R. Uthayakumar, "Fractal model for blood flow in cardiovascular system," *Comput. Biol. Med.*, vol. 38, no. 6, pp. 684–693, Jun. 2008. [Online]. Available: https://www.sciencedirect.com/science/article/pii/S0010482508000498
- [32] J. Ji, A. Zou, J. Liu, C. Yang, X. Zhang, and Y. Song, "A survey on brain effective connectivity network learning," *IEEE Trans. Neural Netw. Learn.* Syst., vol. 34, no. 4, pp. 1879–1899, Apr. 2023.



- [33] Y. Ji, Y. Ji, Y. Liu, Y. Zhao, and L. Zhang, "Research progress on diagnosing retinal vascular diseases based on artificial intelligence and fundus images," *Frontiers Cell Develop. Biol.*, vol. 11, Mar. 2023, Art. no. 1168327.
- [34] B. Jie, M. Liu, D. Zhang, and D. Shen, "Sub-network kernels for measuring similarity of brain connectivity networks in disease diagnosis," *IEEE Trans. Image Process.*, vol. 27, no. 5, pp. 2340–2353, May 2018.
- [35] C. Junliang, "CNN or RNN: Review and experimental comparison on image classification," in *Proc. IEEE 8th Int. Conf. Comput. Commun.* (ICCC), Dec. 2022, pp. 1939–1944.
- [36] H. Kamada, M. Nakamura, H. Ota, S. Higuchi, and K. Takase, "Blood flow analysis with computational fluid dynamics and 4D-flow MRI for vascular diseases," J. Cardiology, vol. 80, no. 5, pp. 386–396, Nov. 2022. [Online]. Available: https://www.sciencedirect.com/science/article/pii/S0914508722001228
- [37] T. Katayama, K. Takahashi, Y. Shimomura, and H. Takizawa, "XAI-based feature importance analysis on loop optimization," in *Proc. IEEE Int. Parallel Distrib. Process. Symp. Workshops (IPDPSW)*, May 2024, pp. 782–791.
- [38] C. Laghridat, M. Essalih, and I. Mounir, "The use of image graph in the medical data analyzing," in *Proc. IEEE Int. Conf. Adv. Data-Driven Analytics Intell. Syst. (ADACIS)*, Nov. 2023, pp. 1–5.
- [39] S. Li, S. Chen, H. Li, G. Ruan, S. Ren, T. Zhang, L. Liu, and H. Chen, "Anatomical point-of-interest detection in head MRI using multipoint feature descriptor," *IEEE Access*, vol. 8, pp. 173239–173249, 2020.
- [40] Y. Li, R. Shafipour, G. Mateos, and Z. Zhang, "Mapping brain structural connectivities to functional networks via graph encoder–decoder with interpretable latent embeddings," in *Proc. IEEE Global Conf. Signal Inf. Process.* (GlobalSIP), Nov. 2019, pp. 1–5.
- [41] A. Lin, M. Kolossváry, M. Motwani, I. Išgum, P. Maurovich-Horvat, P. J. Slomka, and D. Dey, "Artificial intelligence in cardiovascular CT: Current status and future implications," *J. Cardiovascular Comput. Tomogr.*, vol. 15, no. 6, pp. 462–469, Nov. 2021. [Online]. Available: https://www.sciencedirect.com/science/article/pii/S1934592521000368
- [42] J. Liu, Y. Liu, and F. Zhang, "Research and future challenges of radiomics," in *Proc. 14th Int. Conf. Comput. Res. Develop. (ICCRD)*, Jan. 2022, pp. 340–344.
- [43] J. Long, Y. Xie, P. Yuan, and Y. Zhang, "Vessel-guided and graph-based retinal vessel junction detection and classification," *Expert Syst. Appl.*, vol. 275, May 2025, Art. no. 126927. [Online]. Available: https://www.sciencedirect.com/science/article/pii/S0957417425005494
- [44] T. Lorimer, K. Kanders, and R. Stoop, "Natural data structure extracted from neighborhood-similarity graphs," *Chaos, Solitons Fractals*, vol. 119, pp. 326–331, Feb. 2019. [Online]. Available: https://www.sciencedirect.com/science/article/pii/S0960077919300104
- [45] C. Luo, X. Li, L. Wang, J. He, D. Li, and J. Zhou, "How does the data set affect CNN-based image classification performance?" in *Proc. 5th Int. Conf. Syst. Informat. (ICSAI)*, Nov. 2018, pp. 361–366.
- [46] C. Martin-Isla, V. M. Campello, C. Izquierdo, Z. Raisi-Estabragh, B. Baeßler, S. E. Petersen, and K. Lekadir, "Image-based cardiac diagnosis with machine learning: A review," Frontiers Cardiovascular Med., vol. 7, Jan. 2020. [Online]. Available: https://www.frontiersin.org/articles/10.3389/fcvm.2020.00001
- [47] G. Masuno, R. Nagaoka, A. Omori, Y. Ishikawa, O. Akagawa, M. Arakawa, and Y. Saijo, "Two-dimensional blood flow vectors obtained with bidirectional Doppler ultrasound," in *Proc. 36th Annu. Int. Conf. IEEE Eng. Med. Biol. Soc.*, Aug. 2014, pp. 5093–5096.
- [48] M. Ménoret, N. Farrugia, B. Pasdeloup, and V. Gripon, "Evaluating graph signal processing for neuroimaging through classification and dimensionality reduction," in *Proc. IEEE Global Conf. Signal Inf. Process.* (GlobalSIP), Nov. 2017, pp. 618–622.
- [49] M. Mokan, G. Gabrani, and D. Relan, "Pixel-wise classification of the whole retinal vasculature into arteries and veins using supervised learning," *Biomed. Signal Process. Control*, vol. 106, Aug. 2025, Art. no. 107691. [Online]. Available: https://www.sciencedirect.com/science/article/pii/S1746809425002022
- [50] M. Mousavi and N. Khalili, "VSI: An interpretable Bayesian feature selection method based on vendi score," *Knowl.-Based Syst.*, vol. 311, Feb. 2025, Art. no. 112973. [Online]. Available: https://www.sciencedirect.com/science/article/pii/S0950705125000218
- [51] M. Mujat, R. D. Ferguson, D. X. Hammer, A. H. Patel, and N. Iftimia, "High-resolution retinal imaging: Technology overview and applications," *Photonics*, vol. 11, no. 6, p. 522, May 2024.

- [52] R. Nakanishi et al., "Rationale and design of the INVICTUS registry: (Multicenter registry of invasive and non-invasive imaging modalities to compare coronary computed tomography angiography, intravascular ultrasound and optical coherence tomography for the determination of severity, volume and type of coronary atherosclerosiS)," J. Cardiovascular Comput. Tomogr., vol. 17, no. 6, pp. 401–406, Nov. 2023. [Online]. Available: https://www.sciencedirect.com/science/article/pii/S1934592523004276
- [53] T. Nguyen, M. Q. T. Hoang, L. T. Vu, D. T. Ho, T. Cao, E. Talarico, and G. Rigatelli, "Dilated cardiomyopathy delayed progression of atherosclerosis; however, could trigger sudden cardiac death due to functional ischemia: A new coronary imaging, artificial intelligence algorithm, and machine learning program analysis," *Cardiovascular Revascularization Med.*, vol. 40, pp. 76–77, Jul. 2022. [Online]. Available: https://www.sciencedirect.com/science/article/pii/S1553838922005218
- [54] U. F. Njoku, A. Abelló, B. Bilalli, and G. Bontempi, "On many-objective feature selection and the need for interpretability," *Expert Syst. Appl.*, vol. 267, Apr. 2025, Art. no. 126191. [Online]. Available: https://www.sciencedirect.com/science/article/pii/S0957417424030586
- [55] Univ. Auckland. Morphological Image Processing. Accessed: Jul. 10, 2023. [Online]. Available: https://www.cs.auckland.ac.nz/courses/compsci773s1c/lectures/ImageProcessing-html/topic4.htm
- [56] N. Pospelov, E. Levchenko, V. Tiselko, R. Safronova, I. Zakharov, V. Sotskov, and K. Anokhin, "Network entropy analysis reveals high heterogeneity of human functional networks," in *Proc. 6th Scientific School Dyn. Complex Netw. Appl. (DCNA)*, Sep. 2022, pp. 226–229.
- [57] F. Prinzi, C. Militello, N. Scichilone, S. Gaglio, and S. Vitabile, "Explainable machine-learning models for COVID-19 prognosis prediction using clinical, laboratory and radiomic features," *IEEE Access*, vol. 11, pp. 121492–121510, 2023.
- [58] J.-J. Qiu, J. Yin, W. Qian, J.-H. Liu, Z.-X. Huang, H.-P. Yu, L. Ji, and X.-X. Zeng, "A novel multiresolution-statistical texture analysis architecture: Radiomics-aided diagnosis of PDAC based on plain CT images," *IEEE Trans. Med. Imag.*, vol. 40, no. 1, pp. 12–25, Jan. 2021.
- [59] A. Rahmim, A. Toosi, M. R. Salmanpour, N. Dubljevic, I. Janzen, I. Shiri, M. A. Ramezani, R. Yuan, C. Ho, H. Zaidi, C. MacAulay, C. Uribe, and F. Yousefirizi, "Tensor radiomics: Paradigm for systematic incorporation of multi-flavoured radiomics features," in *Proc. IEEE Nucl. Sci. Symp. Med. Imag. Conf. (NSS/MIC)*, Nov. 2022, pp. 1–4.
- [60] P. Rai, S. Jangir, and T. Singh Bal, "Device for ECG prediction based on retinal vasculature analysis," 2020, arXiv:2009.11099.
- [61] R. Razavi, G. Plonka, and H. Rabbani, "X-let's atom combinations for modeling and denoising of OCT images by modified morphological component analysis," *IEEE Trans. Med. Imag.*, vol. 43, no. 2, pp. 760–770, Feb. 2024.
- [62] M. Rubinov and O. Sporns, "Complex network measures of brain connectivity: Uses and interpretations," *NeuroImage*, vol. 52, no. 3, pp. 1059–1069, Sep. 2010. [Online]. Available: https://www.sciencedirect.com/science/article/pii/S105381190901074X
- [63] P. S. Dharshini, R. Kumar, S. Venkatesh, K. Narasimhan, and K. Adalarasu, "An overview of interpretability techniques for explainable artificial intelligence (XAI) in deep learning-based medical image analysis," in *Proc. 9th Int. Conf. Adv. Comput. Commun. Syst. (ICACCS)*, vol. 1, Mar. 2023, pp. 175–182.
- [64] A. M. Salih, I. B. Galazzo, Z. Raisi-Estabragh, S. E. Petersen, G. Menegaz, and P. Radeva, "Characterizing the contribution of dependent features in XAI methods," *IEEE J. Biomed. Health Informat.*, vol. 28, no. 11, pp. 6466–6473, Nov. 2024.
- [65] A. Santhoshi and A. Muthukumaravel, "Texture and shape-based feature extraction for colorectal tumor segmentation," in *Proc. 10th Int. Conf. Adv. Comput. Commun. Syst. (ICACCS)*, Mar. 2024, pp. 315–320.
- [66] R. Saravanan and P. Sujatha, "A state of art techniques on machine learning algorithms: A perspective of supervised learning approaches in data classification," in *Proc. 2nd Int. Conf. Intell. Comput. Control Syst.* (ICICCS), Jun. 2018, pp. 945–949.
- [67] C. Savas and F. Dovis, "Comparative performance study of linear and Gaussian kernel SVM implementations for phase scintillation detection," in *Proc. Int. Conf. Localization GNSS (ICL-GNSS)*, Jun. 2019, pp. 1–6.
- [68] T. H. Schindler et al., "Myocardial perfusion pet for the detection and reporting of coronary microvascular dysfunction: A JACC: Cardiovascular imaging expert panel statement," JACC, Cardiovascular Imag., vol. 16, no. 4, pp. 536–548, 2023. [Online]. Available: https://www.sciencedirect.com/science/article/pii/S1936878X22007446



- [69] L. Schmetterer and D. Gherghel, "Editorial: Vascular involvement in eye diseases," Frontiers Med., vol. 10, Jan. 2024, Art. no. 1301145.
- [70] M. Shafiq-ul-Hassan, G. G. Zhang, K. Latifi, G. Ullah, D. C. Hunt, Y. Balagurunathan, M. A. Abdalah, M. B. Schabath, D. G. Goldgof, D. Mackin, L. E. Court, R. J. Gillies, and E. G. Moros, "Intrinsic dependencies of CT radiomic features on voxel size and number of gray levels," *Med. Phys.*, vol. 44, no. 3, pp. 1050–1062, Mar. 2017, doi: 10.1002/mp.12123. [Online]. Available: https://aapm.onlinelibrary.wiley.com/doi/abs/10.1002/mp.12123
- [71] R. Shaha, D. Talukder, M. A. Iqbal, and M. M. Haque, "TOS: A relative metric approach for model selection in machine learning solutions," in Proc. IEEE Int. Conf. Robot., Autom., Artificial-Intelligence Internet-of-Things (RAAICON), Dec. 2021, pp. 26–31.
- [72] Md. A. B. Siddique, R. B. Arif, and M. M. R. Khan, "Digital image segmentation in MATLAB: A brief study on OTSU's image thresholding," in *Proc. Int. Conf. Innov. Eng. Technol. (ICIET)*, Dec. 2018, pp. 1–5.
- [73] P. N. Srinivasu, N. Sandhya, R. H. Jhaveri, and R. Raut, "From blackbox to explainable AI in healthcare: Existing tools and case studies," *Mobile Inf. Syst.*, vol. 2022, pp. 1–20, Jun. 2022.
- [74] F. J. Tehrani, B. Nasihatkon, K. Al-Qawasmi, M. R. Al-Mousa, and R. Boostani, "An efficient classifier: Kernel SVM-LDA," in *Proc. Int. Eng. Conf. Electr.*, Nov. 2022, pp. 1–4.
- [75] Y. Wang, J. Zhang, M. Cavichini, D. G. Bartsch, W. R. Freeman, T. Q. Nguyen, and C. An, "Robust content-adaptive global registration for multimodal retinal images using weakly supervised deep-learning framework," *IEEE Trans. Image Process.*, vol. 30, pp. 3167–3178, 2021.
- [76] B. D. Wichtmann, F. N. Harder, K. Weiss, S. O. Schönberg, U. I. Attenberger, H. Alkadhi, D. P. dos Santos, and B. Baeßler, "Influence of image processing on radiomic features from magnetic resonance imaging," *Investigative Radiol.*, vol. 58, no. 3, pp. 199–208, Mar. 2023.
- [77] K. P. Win and Y. Kitjaidure, "Biomedical images stitching using ORB feature based approach," in *Proc. Int. Conf. Intell. Informat. Biomed. Sci.* (ICIIBMS), vol. 3, Oct. 2018, pp. 221–225.
- [78] K. Wisaeng, "Retinal blood-vessel extraction using weighted kernel fuzzy C-Means clustering and dilation-based functions," *Diagnostics*, vol. 13, no. 3, p. 342, Jan. 2023, doi: 10.3390/diagnostics13030342.
- [79] C. Wu, Y. He, J. Li, X. Qiu, Q. Zou, and J. Wang, "A novel method for functional brain networks based on static cerebral blood flow," *NeuroImage*, vol. 308, Mar. 2025, Art. no. 121069. [Online]. Available: https://www.sciencedirect.com/science/article/pii/S1053811925000710
- [80] R. Xie, J. Liu, R. Cao, C. S. Qiu, J. Duan, J. Garibaldi, and G. Qiu, "End-to-end fovea localisation in colour fundus images with a hierarchical deep regression network," *IEEE Trans. Med. Imag.*, vol. 40, no. 1, pp. 116–128, Jan. 2021.
- [81] M. Challa, "A comparative analysis of explainable AI techniques for enhanced model interpretability," in *Proc. 3rd Int. Conf. Pervasive Comput. Social Netw. (ICPCSN)*, Jun. 2023, pp. 229–234.
- [82] S. Yaegashi, M. Maeda, R. Nagaoka, and Y. Saijo, "Estimation of three-dimensional blood flow with ultrasound–continuity equation on multiplane dual-angle Doppler imaging," in *Proc. 40th Annu. Int. Conf. IEEE Eng. Med. Biol. Soc. (EMBC)*, Jul. 2018, pp. 3173–3176.
- [83] Y. Yamagata, T. Miyahara, Y. Suzuki, T. Uchida, F. Tokuhara, and T. Kuboyama, "Acquisition of multiple graph structured patterns by an evolutionary method using sets of TTSP graph patterns as individuals," in *Proc. 6th IIAI Int. Congr. Adv. Appl. Informat. (IIAI-AAI)*, Jul. 2017, pp. 459–464.
- [84] D. Yan, Q. Li, C.-W. Lin, J.-Y. Shieh, W.-C. Weng, and P.-H. Tsui, "Hybrid QUS radiomics: A multimodal-integrated quantitative ultrasound radiomics for assessing ambulatory function in Duchenne muscular dystrophy," *IEEE J. Biomed. Health Informat.*, vol. 28, no. 2, pp. 835–845, Feb. 2024.
- [85] H. Yang, "Graphic image segmentation method based on high-precision and fast algorithm," in *Proc. Global Conf. Inf. Technol. Commun.* (GCITC), Dec. 2023, pp. 1–4.
- [86] L. Yu and H. Liu, "Feature selection for high-dimensional data: A fast correlation-based filter solution," in *Proc. ICML*, vol. 2, Jan. 2003, pp. 856–863.
- [87] Y. Zang and L. Fiondella, "A network reliability analysis method for complex systems based on complex network theory," in *Proc. Annu. Rel. Maintainability Symp. (RAMS)*, Jan. 2022, pp. 1–6.
- [88] V. Zarikas and S. V. Georgakopoulos, "Interpretable medical image diagnosis methodology using convolutional neural networks and Bayesian networks," in *Proc. 9th Int. Conf. Math. Comput. Sci. Ind. (MCSI)*, Aug. 2024, pp. 128–133.

- [89] J. Zhang, B. Wen, F. G. P. Kalaw, M. Cavichini, D.-U.-G. Bartsch, W. R. Freeman, T. Q. Nguyen, and C. An, "Accurate registration between ultra-wide-field and narrow angle retina images with 3D eyeball shape optimization," in *Proc. IEEE Int. Conf. Image Process. (ICIP)*, Oct. 2023, pp. 2750–2754.
- [90] X. Zhang, Y. Zhang, G. Zhang, X. Qiu, W. Tan, X. Yin, and L. Liao, "Deep learning with radiomics for disease diagnosis and treatment: Challenges and potential," *Frontiers Oncol.*, vol. 12, Feb. 2022.
- [91] Y. Zhang, L. Gao, K. Shen, K. Zhang, J. Yan, W. Cheng, and J. Zhang, "A simulator for mixed Doppler ultrasound signals from pulsatile blood flow and vessel wall with mild stenosis," in *Proc. 35th Annu. Int. Conf. IEEE Eng. Med. Biol. Soc. (EMBC)*, Jul. 2013, pp. 1903–1906.
- [92] Q. Zhu, R. Xu, R. Wang, X. Xu, Z. Zhang, and D. Zhang, "Stacked topological preserving dynamic brain networks representation and classification," *IEEE Trans. Med. Imag.*, vol. 41, no. 11, pp. 3473–3484, Nov. 2022.

OFÉLIO JORREIA received the degree in computer science from the Pedagogical University of Mozambique and the master's degree in technologies, systems, and communication networks from the Polytechnic University of Valencia, Spain. He is currently pursuing the Ph.D. degree in electrical engineering and intelligent systems with the Institute of Systems and Robotics, University of Coimbra.

He collaborated with the research group at the Instituto de Tecnologias y Aplicaciones Multimedia de Valncia, focusing on the early diagnosis of brain diseases, such as Alzheimer's and schizophrenia through computational intelligence applied to functional magnetic resonance imaging (fMRI). He was a Lecturer with the Pedagogical University of Mozambique and Rovuma University.

NUNO GONÇALVES (Member, IEEE) received the M.Sc. and Ph.D. degrees from the University of Coimbra, in 2002 and 2008, respectively.

He is a Researcher with the Institute of Systems and Robotics, University of Coimbra; and a Tenured Assistant Professor with the Department of Electrical and Computers Engineering, University of Coimbra. Since 2018, he has been the Innovation Manager with INCM. He has scientific publications in visual coding (machine-readable codes), steganography, object recognition, facial recognition and diagnosis, biometrics, documents security, augmented and virtual reality, reflections for image rendering, light field cameras, omnidirectional vision, non-central cameras, calibration, optics, camera models, motion estimation, pose estimation, web information systems, sports vision, and legged robotics. He was the principal investigator of a closed project, funded by Portuguese Science and Technology Foundation, in non-central camera models for computer graphics and computer-aided surgery. He is currently a Scientific Coordinator of several projects with the industry (funded by INCM-Portuguese Mint and Official Printing Office) in the area of security elements involving biometrics, machine readable codes (with some applications in virtual and augmented reality), security unique marks in printing labels, security unique marks in assay contrasts in artifacts of precious metals, and processing of human faces in 3-D by using several types of cameras. He is an inventor of six patents. His main research interests include computer vision, biometrics, machinereadable codes, security printing, computer graphics and machine learning, with special emphasis to biometrics and steganography for ID and travel documents.

RUI CORTESÃO (Member, IEEE) received the B.Sc. (Licenciatura) degree in electrical engineering, the M.Sc. degree in systems and automation, and the Ph.D. degree in control and instrumentation from the University of Coimbra, Coimbra, Portugal, in 1994, 1997, and 2003, respectively. He was a Visiting Researcher with German Aerospace Center (DLR), Oberpfaffenhofen, Germany, from 1998 to 2003. He did his Ph.D. work with Stanford University, Stanford, CA, USA, in 2002; LIRMM-CNRS, Montpellier, France, in 2004, 2006, and 2008; Barrett Technologies, Boston, MA, USA, in 2007; and Trinity College, Dublin, Ireland, in 2018, having worked on surgical robotics, haptic tele-manipulation, compliant motion control, data fusion, and human-robot skill transfer. He is currently a Professor with the University of Coimbra; the Head of the Medical Robotics Group, Institute of Systems and Robotics (ISR-UC); and the Director of the Technology Transfer Laboratory, IPN-LAS.

. . .